

Silicon on-chip 1D photonic crystal nanobeam bandstop filters for the parallel multiplexing of ultra-compact integrated sensor array

DAQUAN YANG,^{1,2,4} CHUAN WANG,^{2,5} AND YUEFENG JI^{1,2,3,6}

¹*School of information and communication Engineering, Beijing University of Posts and Telecommunications, Beijing 100876, China*

²*State Key Laboratory of Information Photonics and Optical Communications, Beijing University of Posts and Telecommunications, Beijing 100876, China*

³*Beijing Advanced Innovation Center for Future Internet Technology, Beijing University of Technology, Beijing 100124, China.*

⁴*yangdq5896@163.com*

⁵*wangchuan@bupt.edu.cn*

⁶*jyf@bupt.edu.cn*

Abstract: We propose a novel multiplexed ultra-compact high-sensitivity one-dimensional (1D) photonic crystal (PC) nanobeam cavity sensor array on a monolithic silicon chip, referred to as Parallel Integrated 1D PC Nanobeam Cavity Sensor Array (PI-1DPC-NCSA). The performance of the device is investigated numerically with three-dimensional finite-difference time-domain (3D-FDTD) technique. The PI-1DPC-NCSA consists of multiple parallel-connected channels of integrated 1D PC nanobeam cavities/waveguides with gap separations. On each channel, by connecting two additional 1D PC nanobeam bandstop filters (1DPC-NBFs) to a 1D PC nanobeam cavity sensor (1DPC-NCS) in series, a transmission spectrum with a single targeted resonance is achieved for the purpose of multiplexed sensing applications. While the other spurious resonances are filtered out by the stop-band of 1DPC-NBF, multiple 1DPC-NCSs at different resonances can be connected in parallel without spectrum overlap. Furthermore, in order for all 1DPC-NCSs to be integrated into microarrays and to be interrogated simultaneously with a single input/output port, all channels are then connected in parallel by using a $1 \times n$ taper-type equal power splitter and a $n \times 1$ S-type power combiner in the input port and output port, respectively (n is the channel number). The concept model of PI-1DPC-NCSA is displayed with a 3-parallel-channel 1DPC-NCSs array containing series-connected 1DPC-NBFs. The bulk refractive index sensitivities as high as 112.6nm/RIU, 121.7nm/RIU, and 148.5nm/RIU are obtained (RIU = Refractive Index Unit). In particular, the footprint of the 3-parallel-channel PI-1DPC-NCSA is $4.5\mu\text{m} \times 50\mu\text{m}$ (width \times length), decreased by more than three orders of magnitude compared to 2D PC integrated sensor arrays. Thus, this is a promising platform for realizing ultra-compact lab-on-a-chip applications with high integration density and high parallel-multiplexing capabilities.

©2016 Optical Society of America

OCIS codes: (130.6010) Sensors; (130.3120) Integrated optics devices; (130.6622) Subsystem integration and techniques; (160.5298) Photonic crystals; (200.4650) Optical interconnects; (060.4230) Multiplexing.

References and links

1. R. Daw and J. Finkelstein, "Lab on a chip," *Nature* **442**(7101), 367–418 (2006).
2. H. K. Hunt and A. M. Armani, "Label-free biological and chemical sensors," *Nanoscale* **2**(9), 1544–1559 (2010).
3. X. Fan, I. M. White, S. I. Shopova, H. Zhu, J. D. Suter, and Y. Sun, "Sensitive optical biosensors for unlabeled targets: a review," *Anal. Chim. Acta* **620**(1-2), 8–26 (2008).
4. Y. Liu, S. Chen, Q. Liu, J. F. Masson, and W. Peng, "Compact multi-channel surface plasmon resonance sensor for real-time multi-analyte biosensing," *Opt. Express* **23**(16), 20540–20548 (2015).
5. M. D. Baaske, M. R. Foreman, and F. Vollmer, "Single-molecule nucleic acid interactions monitored on a label-free microcavity biosensor platform," *Nat. Nanotechnol.* **9**(11), 933–939 (2014).
6. J. N. Anker, W. P. Hall, O. Lyandres, N. C. Shah, J. Zhao, and R. P. Van Duyne, "Biosensing with plasmonic nanosensors," *Nat. Mater.* **7**(6), 442–453 (2008).
7. R. Karlsson, "SPR for molecular interaction analysis: a review of emerging application areas," *J. Mol. Recognit.* **17**(3), 151–161 (2004).

8. B. B. Li, W. R. Clements, X. C. Yu, K. Shi, Q. Gong, and Y. F. Xiao, "Single nanoparticle detection using split-mode microcavity Raman lasers," *Proc. Natl. Acad. Sci. U.S.A.* **111**(41), 14657–14662 (2014).
9. R. Liu, W. Jin, X. Yu, Y. Liu, and Y. Xiao, "Enhanced Raman scattering of single nanoparticles in a high-Q whispering-gallery microresonator," *Phys. Rev. A* **91**(4), 043836 (2015).
10. Ş. K. Özdemir, J. Zhu, X. Yang, B. Peng, H. Yilmaz, L. He, F. Monifi, S. H. Huang, G. L. Long, and L. Yang, "Highly sensitive detection of nanoparticles with a self-referenced and self-heterodyned whispering-gallery Raman microlaser," *Proc. Natl. Acad. Sci. U.S.A.* **111**(37), E3836–E3844 (2014).
11. J. Zhu, S. Ozdemir, Y. Xiao, L. Li, L. He, D. Chen, and L. Yang, "On-chip single nanoparticle detection and sizing by mode splitting in an ultrahigh-Q microresonator," *Nat. Photonics* **4**(1), 46–49 (2010).
12. L. He, S. K. Özdemir, J. Zhu, W. Kim, and L. Yang, "Detecting single viruses and nanoparticles using whispering gallery microlasers," *Nat. Nanotechnol.* **6**(7), 428–432 (2011).
13. S. Arnold, S. I. Shopova, and S. Holler, "Whispering gallery mode bio-sensor for label-free detection of single molecules: thermo-optic vs. reactive mechanism," *Opt. Express* **18**(1), 281–287 (2010).
14. K. Misiakos, I. Raptis, A. Salapatas, E. Makarona, A. Botsialas, M. Hoekman, R. Stoffer, and G. Jobst, "Broad-band Mach-Zehnder interferometers as high performance refractive index sensors: Theory and monolithic implementation," *Opt. Express* **22**(8), 8856–8870 (2014).
15. A. Ymeti, J. Greve, P. V. Lambeck, T. Wink, S. W. van Hövell, T. A. M. Beumer, R. R. Wijn, R. G. Heideman, V. Subramaniam, and J. S. Kanger, "Fast, ultrasensitive virus detection using a Young interferometer sensor," *Nano Lett.* **7**(2), 394–397 (2007).
16. B. J. Luff, J. S. Wilkinson, J. Piehler, U. Hollenbach, J. Ingenhoff, and N. Fabricius, "Integrated optical Mach-Zehnder biosensor," *J. Lightwave Technol.* **16**(4), 583–592 (1998).
17. C. J. Smith, R. Shankar, M. Laderer, M. B. Frish, M. Loncar, and M. G. Allen, "Sensing nitrous oxide with QCL-coupled silicon-on-sapphire ring resonators," *Opt. Express* **23**(5), 5491–5499 (2015).
18. X. Fan and I. M. White, "Optofluidic microsystems for chemical and biological analysis," *Nat. Photonics* **5**(10), 591–597 (2011).
19. K. De Vos, J. Girones, T. Claes, Y. De Koninck, S. Popelka, E. Schacht, R. Baets, and P. Bienstman, "Multiplexed antibody detection with an array of silicon-on-insulator microring resonators," *IEEE Photonics J.* **1**(4), 225–235 (2009).
20. M. S. Kwon and W. H. Steier, "Microring-resonator-based sensor measuring both the concentration and temperature of a solution," *Opt. Express* **16**(13), 9372–9377 (2008).
21. J. T. Robinson, L. Chen, and M. Lipson, "On-chip gas detection in silicon optical microcavities," *Opt. Express* **16**(6), 4296–4301 (2008).
22. A. Ramachandran, S. Wang, J. Clarke, S. J. Ja, D. Goad, L. Wald, E. M. Flood, E. Knobbe, J. V. Hryniewicz, S. T. Chu, D. Gill, W. Chen, O. King, and B. E. Little, "A universal biosensing platform based on optical microring resonators," *Biosens. Bioelectron.* **23**(7), 939–944 (2008).
23. A. Yalcin, K. Papat, J. Aldridge, T. Desai, J. Hryniewicz, N. Chbouki, B. E. Little, V. Van, D. Gill, M. Anthes-Washburn, M. Unlu, and B. Goldberg, "Optical sensing of biomolecules using microring resonator," *IEEE J. Sel. Top. Quantum Electron.* **12**(1), 148–155 (2006).
24. M. Lončar, A. Scherer, and Y. Qiu, "Photonic crystal cavity laser sources for chemical detection," *Appl. Phys. Lett.* **82**(26), 4648–4651 (2003).
25. J. Topolancik, P. Bhattacharya, J. Sabarinathan, and P. Yu, "Fluid detection with photonic crystal-based multichannel waveguides," *Appl. Phys. Lett.* **82**(8), 1143–1145 (2003).
26. E. Chow, A. Grot, L. W. Mirkarimi, M. Sigalas, and G. Girolami, "Ultracompact biochemical sensor built with two-dimensional photonic crystal microcavity," *Opt. Lett.* **29**(10), 1093–1095 (2004).
27. N. Skivesen, A. Têtù, M. Kristensen, J. Kjems, L. H. Frandsen, and P. I. Borel, "Photonic-crystal waveguide biosensor," *Opt. Express* **15**(6), 3169–3176 (2007).
28. M. R. Lee and P. M. Fauchet, "Two-dimensional silicon photonic crystal based biosensing platform for protein detection," *Opt. Express* **15**(8), 4530–4535 (2007).
29. S. Kita, K. Nozaki, and T. Baba, "Refractive index sensing utilizing a cw photonic crystal nanolaser and its array configuration," *Opt. Express* **16**(11), 8174–8180 (2008).
30. S. H. Kwon, T. Stünner, M. Kamp, and A. Forchel, "Optimization of photonic crystal cavity for chemical sensing," *Opt. Express* **16**(16), 11709–11717 (2008).
31. A. Di Falco, L. O'Faolain, and T. F. Krauss, "Chemical sensing in slotted photonic crystal heterostructure cavities," *Appl. Phys. Lett.* **94**(6), 063503 (2009).
32. S. Tomljenovic-Hanic, A. Rahmani, M. J. Steel, and C. M. de Sterke, "Comparison of the sensitivity of air and dielectric modes in photonic crystal slab sensors," *Opt. Express* **17**(17), 14552–14557 (2009).
33. T. Xu, N. Zhu, M. Y. Xu, L. Wosinski, J. S. Aitchison, and H. E. Ruda, "Pillar-array based optical sensor," *Opt. Express* **18**(6), 5420–5425 (2010).
34. T. W. Lu, Y. H. Hsiao, W. D. Ho, and P. T. Lee, "High-index sensitivity of surface mode in photonic crystal hetero-slab-edge microcavity," *Opt. Lett.* **35**(9), 1452–1454 (2010).
35. M. G. Scullion, A. Di Falco, and T. F. Krauss, "Slotted photonic crystal cavities with integrated microfluidics for biosensing applications," *Biosens. Bioelectron.* **27**(1), 101–105 (2011).
36. Y. Liu and H. W. M. Salemink, "Photonic crystal-based all-optical on-chip sensor," *Opt. Express* **20**(18), 19912–19920 (2012).
37. S. Hachuda, S. Otsuka, S. Kita, T. Isono, M. Narimatsu, K. Watanabe, Y. Goshima, and T. Baba, "Selective detection of sub-atto-molar Streptavidin in 10(13)-fold impure sample using photonic crystal nanolaser sensors," *Opt. Express* **21**(10), 12815–12821 (2013).

38. A. Casas-Bedoya, S. Shahnian, D. Di Battista, E. Mägi, and B. J. Eggleton, "Chip scale humidity sensing based on a microfluidic infiltrated photonic crystal," *Appl. Phys. Lett.* **103**(18), 181109 (2013).
39. H. Lu, B. Sadani, G. Ulliac, C. Guyot, N. Courjal, M. Collet, F. I. Baida, and M. P. Bernal, "Integrated temperature sensor based on an enhanced pyroelectric photonic crystal," *Opt. Express* **21**(14), 16311–16318 (2013).
40. M. N. Hossain, J. Justice, P. Lovera, A. O'Riordan, and B. Corbett, "Dual resonance approach to decoupling surface and bulk attributes in photonic crystal biosensor," *Opt. Lett.* **39**(21), 6213–6216 (2014).
41. C. Caër, S. F. Serna-Otálvaro, W. Zhang, X. Le Roux, and E. Cassan, "Liquid sensor based on high-Q slot photonic crystal cavity in silicon-on-insulator configuration," *Opt. Lett.* **39**(20), 5792–5794 (2014).
42. P. G. Hermansson, K. T. Sørensen, C. Vannahme, C. L. Smith, J. J. Klein, M. M. Russew, G. Grützner, and A. Kristensen, "All-polymer photonic crystal slab sensor," *Opt. Express* **23**(13), 16529–16539 (2015).
43. A. A. Siraji and Y. Zhao, "High-sensitivity and high-Q-factor glass photonic crystal cavity and its applications as sensors," *Opt. Lett.* **40**(7), 1508–1511 (2015).
44. V. M. Lavchiev, B. Jakoby, U. Hedenig, T. Grille, J. M. R. Kirkbride, and G. A. D. Ritchie, "M-line spectroscopy on mid-infrared Si photonic crystals for fluid sensing and chemical imaging," *Opt. Express* **24**(1), 262–271 (2016).
45. M. Hameed, M. Azab, A. Heikal, S. El-Hefnawy, and S. Obayya, "Highly sensitive plasmonic photonic crystal temperature sensor filled with liquid crystal," *IEEE Photonics Technol. Lett.* **28**(1), 59–62 (2016).
46. D. Psaltis, S. R. Quake, and C. Yang, "Developing optofluidic technology through the fusion of microfluidics and optics," *Nature* **442**(7101), 381–386 (2006).
47. C. Monat, P. Domachuk, and B. J. Eggleton, "Integrated opto-fluidics: a new river of light," *Nat. Photonics* **1**(2), 106–114 (2007).
48. S. Mandal and D. Erickson, "Nanoscale optofluidic sensor arrays," *Opt. Express* **16**(3), 1623–1631 (2008).
49. S. Pal, E. Guillermain, R. Sriram, B. L. Miller, and P. M. Fauchet, "Silicon photonic crystal nanocavity-coupled waveguides for error-corrected optical biosensing," *Biosens. Bioelectron.* **26**(10), 4024–4031 (2011).
50. D. Yang, H. Tian, and Y. Ji, "Nanoscale photonic crystal sensor arrays on monolithic substrates using side-coupled resonant cavity arrays," *Opt. Express* **19**(21), 20023–20034 (2011).
51. D. Yang, H. Tian, and Y. Ji, "Nanoscale low crosstalk photonic crystal integrated sensor array," *IEEE Photonics J.* **6**, 1–7 (2014).
52. Y. Zou, S. Chakravarty, L. Zhu, and R. T. Chen, "The role of group index engineering in series-connected photonic crystal microcavities for high density sensor microarrays," *Appl. Phys. Lett.* **104**(14), 141103 (2014).
53. J. T. Robinson, C. Manolatu, L. Chen, and M. Lipson, "Ultrascale mode volumes in dielectric optical microcavities," *Phys. Rev. Lett.* **95**(14), 143901 (2005).
54. P. Velha, E. Picard, T. Charvolin, E. Hadji, J. C. Rodier, P. Lalanne, and D. Peyrade, "Ultra-high Q/V fabry-perot microcavity on soi substrate," *Opt. Express* **15**(24), 16090–16096 (2007).
55. J. D. Ryckman and S. M. Weiss, "Low mode volume slotted photonic crystal single nanobeam cavity," *Appl. Phys. Lett.* **101**(7), 071104 (2012).
56. E. Kuramochi, H. Taniyama, T. Tanabe, K. Kawasaki, Y. G. Roh, and M. Notomi, "Ultra-high-Q one-dimensional photonic crystal nanocavities with modulated mode-gap barriers on SiO₂ claddings and on air claddings," *Opt. Express* **18**(15), 15859–15869 (2010).
57. Q. Quan, P. B. Deotare, and M. Loncar, "Photonic crystal nanobeam cavity strongly coupled to the feeding waveguide," *Appl. Phys. Lett.* **96**(20), 203102 (2010).
58. P. B. Deotare, M. W. McCutcheon, I. W. Frank, M. Khan, and M. Loncar, "High quality factor photonic crystal nanobeam cavities," *Appl. Phys. Lett.* **94**(12), 121106 (2009).
59. Y. Li, C. Wang, and M. Loncar, "Design of nano-groove photonic crystal cavities in lithium niobate," *Opt. Lett.* **40**(12), 2902–2905 (2015).
60. A. Bazin, R. Raj, and F. Raineri, "Design of silica encapsulated high-Q photonic crystal nanobeam cavity," *J. Lightwave Technol.* **32**(5), 952–958 (2014).
61. S. Kim, H. M. Kim, and Y. H. Lee, "Single nanobeam optical sensor with a high Q-factor and high sensitivity," *Opt. Lett.* **40**(22), 5351–5354 (2015).
62. T. Lin, X. Zhang, G. Zhou, C. Siong, and J. Deng, "Design of an ultra-compact slotted photonic crystal nanobeam cavity for biosensing," *J. Opt. Soc. Am. B* **32**(9), 1788–1791 (2015).
63. D. Yang, H. Tian, and Y. Ji, "High-Q and high-sensitivity width-modulated photonic crystal single nanobeam air-mode cavity for refractive index sensing," *Appl. Opt.* **54**(1), 1–5 (2015).
64. C. Wang, Q. Quan, S. Kita, Y. Li, and M. Loncar, "Single-nanoparticle detection with slot-mode photonic crystal cavities," *Appl. Phys. Lett.* **106**(26), 261105 (2015).
65. D. Yang, P. Zhang, H. Tian, Y. Ji, and Q. Quan, "Ultra-high-Q and low mode volume parabolic radius-modulated single photonic crystal slot nanobeam cavity for high-sensitive refractive index sensing," *IEEE Photonics J.* **7**, 4501408 (2015).
66. D. Yang, S. Kita, F. Liang, C. Wang, H. Tian, Y. Ji, M. Loncar, and Q. Quan, "High sensitivity and high Q-factor nanoslotted parallel quadrabeam photonic crystal cavity for real-time and label-free sensing," *Appl. Phys. Lett.* **105**(6), 063118 (2014).
67. D. Yang, H. Tian, Y. Ji, and Q. Quan, "Design of simultaneous high-Q and high-sensitivity photonic crystal refractive index sensors," *J. Opt. Soc. Am. B* **30**(8), 2027–2031 (2013).
68. Q. Quan, D. L. Floyd, I. B. Burgess, P. B. Deotare, I. W. Frank, S. K. Y. Tang, R. Ilic, and M. Loncar, "Single particle detection in CMOS compatible photonic crystal nanobeam cavities," *Opt. Express* **21**(26), 32225–32233 (2013).

69. F. Liang, N. Clarke, P. Patel, M. Loncar, and Q. Quan, "Scalable photonic crystal chips for high sensitivity protein detection," *Opt. Express* **21**(26), 32306–32312 (2013).
70. H. Yan, Y. Zou, S. Chakravarty, C. J. Yang, Z. Wang, N. Tang, D. Fan, and R. T. Chen, "Silicon on-chip bandpass filters for the multiplexing of high sensitivity photonic crystal microcavity biosensors," *Appl. Phys. Lett.* **106**(12), 121103 (2015).
71. J. D. Joannopoulos, S. G. Johnson, J. N. Winn, and R. D. Meade, *Photonic Crystals: Molding the Flow of Light*, 2nd ed. (Princeton University Press, 2008).
72. Q. Quan and M. Loncar, "Deterministic design of wavelength scale, ultra-high Q photonic crystal nanobeam cavities," *Opt. Express* **19**(19), 18529–18542 (2011).
73. D. Yang, C. Wang, and Y. Ji, "Silicon on-chip one-dimensional photonic crystal nanobeam bandgap filter integrated with nanobeam cavity for accurate refractive index sensing," *IEEE Photonics J.* **8**(2), 4500608 (2016).

1. Introduction

Lab-on-a-chip ultra-compact and high-sensitivity bio-chemical sensors are very attractive in various applications, such as medical diagnosis, drug development, environmental protection, medicine security, and food safety [1]. While optical sensing techniques represent one of the most popular methods for performing sensitive, real-time and label-free biomolecular detection [2,3]. During the past decades, various different photonic structures with a resonant mode have been developed as optical sensor devices. The most exploited schemes are based on the principles of surface plasmon resonance (SPR) [4–7], whispering-gallery microresonator (WGM) [8–13], Mach-Zehnder interferometer (MZI) [14–16], ring resonator (RR) [17–23], and photonic crystals (PC) [24–45]. Particularly among these, PC based optical sensors show promising advantages in density-integrated sensor array devices for high-parallel multiplexed sensing detections and lab-on-a-chip applications due to their ultra-compact size, small footprints, and high integrability with photonic integrated circuits (PICs) [46,47]. For example, Mandal *et al.* demonstrated a nanoscale opto-fluidic sensor array based on a silicon (*Si*) waveguide with a one-dimensional (1D) PC side-coupled microcavity resonator that lies adjacent to a silicon bus waveguide [48]. Pal *et al.* demonstrated an optical biosensor array based on several series-connected PC microcavity sensor units [49]. Yang *et al.* displayed a two-dimensional (2D) PC integrated sensor array (PC-ISA) based on series-connected H₀ microcavities side-coupled to 2D PC waveguides [50,51]. Zou *et al.* demonstrated a 16-channel 2D PC-ISA based on series-connected L₃ (*Ln*) microcavities side-coupled to 2D PC waveguides [52]. However, most of these PC-ISAs are based on 2D PC platforms. The footprints of these 2D PC-ISAs are usually too large (for example, the full device footprint is ~400μm × 1600μm in [52]), which are not suitable for high density integration. Moreover, for the above mentioned multi-channel 2D PC-ISAs, multiple coupling optical fibers at the output port are necessary in order to monitor the responses (*e.g.* binding reactions) from all PC cavity sensor units simultaneously. And the design limitation of these multi-channel 2D PC-ISAs is that all sensor units cannot be interrogated simultaneously between a single input optical fiber and a single output optical fiber, resulting in the devices packing and alignment to be fragile and cost-expensive.

In order to overcome the above mentioned design drawback and limitation of the 2D PC-ISA platforms, ultra-high Q/V_m (Q = cavity quality factors, and V_m = cavity mode volumes) 1D PC nanobeam cavities (1DPC-NCs) [53–60] have been recently demonstrated as a competitive candidate for nanoscale high-density ISA with ultra-high sensitivity, due to their ultra-compact footprints and high integrability with optical waveguides and circuits. So far, a variety of nanoscale optical cavity sensors based on 1DPC-NCs with ultra-high sensitivities (S) and ultra-high Q-factors (Q) have been demonstrated [61–69]. However, from the practical application perspective, the design limitation of these 1D PC nanobeam cavity sensors (1DPC-NCSs) is that they only typically operate as point or single sensor. And the number of targets which can be screened for at one time is relatively small. Moreover, the long-strip shape 1DPC-NCSs have several resonant wavelengths in the transmission spectrum as shown in previous work [61–69], which makes them difficult to realize highly-parallel and multiplexed sensing on a monolithic silicon chip. Ideally one would like an architecture that combines a high figure of merit (FOM) with the ability to multiplex multiple detection sites

between a single input and output on monolithic substrates, enabling the packing and alignment to be robust and cost-effective.

Herein, towards this direction, a novel method for the dense integration of ultra-compact and high sensitivity 1D PC nanobeam cavity based sensors is proposed on a monolithic silicon chip, which we refer to as Parallel Integrated 1D Photonic Crystal Nanobeam Cavity Sensor Array (PI-1DPC-NCSA). The performance of the device is investigated theoretically by using three-dimensional finite-difference time-domain (3D-FDTD) simulation. The proposed PI-1DPC-NCSA device consists of multiple parallel channels of integrated 1D PC nanobeam cavities/waveguides with gap separations. By connecting two additional 1DPC-NBFs to a 1DPC-NCS in series on each channel, a transmission with a single targeted resonance for sensing purposes is created, while the other spurious resonance modes are filtered out by the stop-band of the series-connected filters. Thus, multiple 1DPC-NCSs at different resonances can be connected in parallel without spectrum overlap.

Furthermore, in order to restrain crosstalk between the channels and to enable all nanobeam sensing units to be interrogated simultaneously by using a single input fiber lens and a single output fiber lens, all channels are then connected in parallel by placing a $1 \times n$ equal power splitter and a $n \times 1$ S-type power combiner in the input and output ports, respectively. When n sensing channels are connected in parallel, the output transmission spectrum will exhibit n resonant peaks. In this work, the conceptual model of the proposed PI-1DPC-NCSA is displayed with a 3-parallel-channel multiplexed 1DPC nanobeam cavity sensor array containing series-connected 1DPC nanobeam bandstop filters. By using 3D-FDTD method, as expected, the composed output transmission only containing three resonant peaks for multiplexed sensing is observed. Moreover, the numerical results show that, as the RI in the region surrounding each sensing channel changed, all the three resonant peak shifts are independent of each other, namely, a shift in one of them does not perturb the others. The numerical calculated RI sensitivities for each sensor unit of the proposed 3-parallel-channel PI-1DPC-NCSA as large as 112.6nm/RIU, 121.7nm/RIU, and 148.5nm/RIU can be achieved. In addition, it is worth mentioning that the total footprint of the proposed 3-parallel-channel multiplexed PI-1DPC-NCSA is ultra-compact of $4.5\mu\text{m} \times 50\mu\text{m}$ (width by length), which decreased by three orders of magnitude compared to the sensor arrays based on 2D PC side-coupled cavities [50–52,70], without sacrificing Q -factors and RI sensitivities.

2. 1DPC-NBFs serially-integrated with 1DPC-NCS to obtain a single targeted resonance

In order to obtain a transmission spectrum of multi-resonance 1DPC-NCS only containing a single targeted resonance, while the other spurious resonances are filtered out at the same time, a novel method for the dense-integration of ultra-compact and high-sensitivity 1DPC waveguide/cavity sensors is presented. Figure 1(a) displays the schematic of the integrated 1D PC nanobeam waveguide/cavity device, which consists of one 1DPC-NCS and two additional serially-connected 1DPC-NBFs.

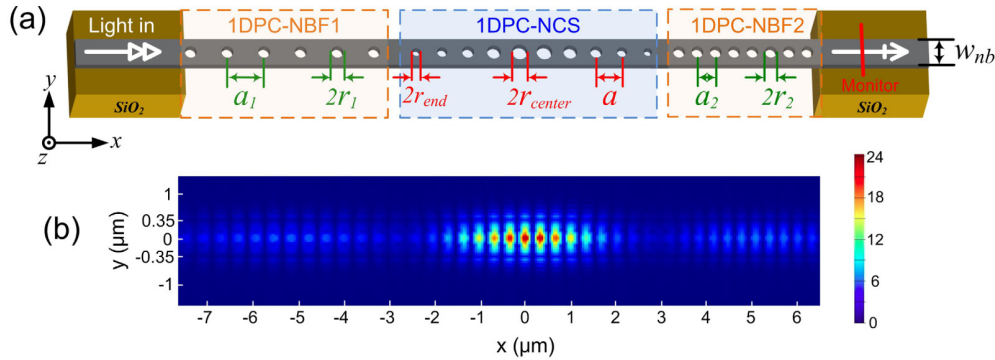


Fig. 1. (a) Schematic of integrated silicon 1D PC nanobeam waveguide/cavity device, which consists of one 1DPC-NCS and two additional serially-connected 1DPC-NBFs. (b) 3D-FDTD simulation of the major field distribution profile ($|E_y|$) of the specific targeted resonant mode ($\sim 1520\text{nm}$) for sensing purpose in the integrated 1D PC nanobeam device formed by two additional series-connected 1DPC-NBFs and a 1DPC-NCS. The unit of the x/y axis is micrometers. Here, for both 1DPC-NBF1 and 1DPC-NBF2, the periodicity $a_1 = 392\text{nm}$ and $a_2 = 304\text{nm}$, the radius of air-hole gratings are kept the same as $r_1 = 90\text{nm}$ and $r_2 = 90\text{nm}$, respectively. For 1DPC-NCS, the periodicity $a = 330\text{nm}$. To create a Gaussian mirror, the air-hole gratings radius are parabolically tapered from $r_{\text{center}} = 121\text{nm}$ in the center to $r_{\text{end}} = 85\text{nm}$ on both sides, which is symmetric with respect to its center. The thickness and width of the silicon nanobeam waveguide is $h = 220\text{nm}$ and $w_{\text{nb}} = 700\text{nm}$. $n_{\text{si}} = 3.46$, $n_{\text{air}} = 1.0$.

Firstly, for both additional serially-connected 1DPC-NBF1 and 1DPC-NBF2 shown in Fig. 1(a), which consists of a 1D PC nanobeam waveguide providing a wide transmission stop-band, the periodicity $a_1 = 392\text{nm}$ and $a_2 = 304\text{nm}$, respectively; and the radius of air-hole gratings are kept the same as $r_1 = r_2 = 90\text{nm}$. The thickness and width of the silicon nanobeam waveguide are $h = 220\text{nm}$ and $w_{\text{nb}} = 700\text{nm}$, respectively. The RI of air-holes and silicon waveguide are $n_{\text{air}} = 1.0$ and $n_{\text{si}} = 3.46$, respectively. By using 3D-FDTD method, Figs. 2(a) and 2(b) show a typical TE band diagram and transmission spectrum of 1DPC-NBF, respectively, with periodicity $a_1 = 392\text{nm}$ and air-hole grating radius $r_1 = 90\text{nm}$. As seen from the transmission spectrum of 1DPC-NBF shown in Fig. 2(b), a wide stop-band over 250nm , ranging from 1533.56nm to 1786.26nm , is observed, which agrees well with the photonic band gap (PBG) ranging from 167.97THz to 195.57THz obtained from band diagram calculation shown in Fig. 2(a). The light with wavelengths in the band-stop region of 1DPC-NBF is not guided. As known in [71], by adjusting the effective refractive index (n_{eff}) of 1DPC-NBF, an arbitrary stop-band can be obtained. Thus, the displayed 1DPC-NBF can be used as an effective bandstop filter to filter out the spurious resonances whose resonant wavelengths lie in the band-stop region.

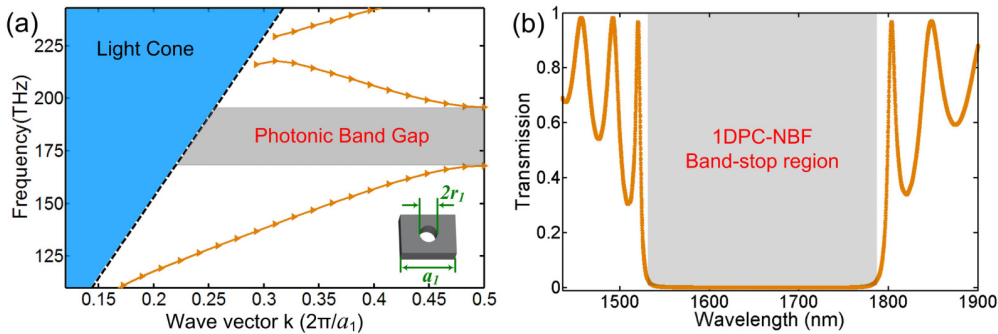


Fig. 2. (a) 3D-FDTD calculated TE band diagram for the 1DPC-NBF1 of Fig. 1(a), a three dimensional dielectric strip, suspended in air, with a period- a_1 sequence of cylindrical air-holes. Only the irreducible Brillouin-zone is shown. The discrete guided modes are labeled by

orange solid line with triangle marks. The light-cone is shaded blue, bounded by the light line in black dashed line. The inset is the unit cell of 1D PC nanobeam waveguide used in the band structure calculation, in which $a_l = 392\text{nm}$, $r_l = 90\text{nm}$, $w_{\text{nb}} = 700\text{nm}$, and $h = 220\text{nm}$. (b) 3D-FDTD calculated transmission spectrum of the displayed 1DPC-NBF device, in which a wide stop-band ranging from 1533.56nm to 1786.26nm is observed.

Secondly, for the displayed 1DPC-NCS in Fig. 1(a), which consists of a typical 1D PC nanobeam cavity with ultra-high Q-factor ($Q > 10^9$) [72], the periodicity $a = 330\text{nm}$, and the air-hole gratings radius are parabolically tapered from $r_{\text{center}} = 0.36a$ nm in the center to $r_{\text{end}} = 0.26a$ on both sides of 1D PC nanobeam cavity, which is symmetric with respect to its center. The thickness and width of the silicon nanobeam waveguide are kept fixed. Based on 3D-FDTD calculations, a typical transmission spectrum of the 1DPC-NCS is shown in Fig. 3(a). As seen, several resonant modes are observed simultaneously in the transmission spectrum. Moreover, these modes are close to each other, which makes them difficult to multiplex because of the overlap/crosstalk among these resonant modes. In order to solve this problem, the resonance filter is created by connecting the 1DPC-NBFs and 1DPC-NCS in series (Fig. 1(a)). Figure 3(b) shows a typical transmission spectrum of the integrated device formed by 1DPC-NCS and one serially-connected 1DPC-NBF1 with a stop-band ranging from 1533nm to 1786nm. As seen, compared to the transmission spectrum of 1DPC-NCS without filters [Fig. 3(a)], a transmission with a single targeted resonant mode for sensing is obtained. As expected, the other spurious resonant modes within the stop-band are filtered out. However, we find that the noise around 1380nm lower than -15dB (noise to signal ratio, NSR) is also introduced due to the additional 1DPC-BNF1. In order to further eliminate the noise around 1380nm, another serially-connected 1DPC-BNF2 with a stop-band ranging from 1300nm to 1500nm is added. The schematic of the whole integrated structure, which consists of one 1DPC-NCS and two serially-connected 1DPC-NBFs, is displayed in Fig. 1(a). With 3D-FDTD method, the corresponding transmission spectrum of the proposed integrated 1D PC nanobeam sensor device is shown in Fig. 3(c). As shown, for wavelengths ranging from 1300nm to 1790nm (bandwidth $\sim 500\text{nm}$), only the selected targeted mode ($\sim 1520\text{nm}$) is observed in the transmission spectrum. Moreover, the series-connected additional 1DPC-NBFs have no effect on the resonant wavelength position of the targeted resonance, which indicates that the method presented here is suitable for multi-resonance 1D PC nanobeam cavity sensor array design. In addition, it should be noted that the series-connected additional 1DPC-NBFs may increase the noise due to the overlapping of oscillations near the cutoff-wavelength edge in the transmission spectra of filters. This problem can be eliminated by optimizing the Q -factors of 1DPC-NCS and optimizing the 1DPC-NBFs design to achieve the transmission spectrum of filters with sharper band edge [73]. Figure 1(b) and Figs. 3(d)-3(f) show the major field distribution profile ($|E_y|$) in x - y plane of the targeted mode in the sensing site of 1DPC-NCS. As shown, a significant amount of electric field is strongly localized within the center of 1DPC-NCS, which makes the sensor very sensitive to RI changes due to the enhancement of light-matter interactions. In addition, the footprint of the integrated sensor device based on 1DPC-NCS and serially-connected 1DPC-BNFs is ultra-compact as $\sim 0.7\mu\text{m} \times 15\mu\text{m}$ (width by length) (Fig. 1), and thus is potentially an ideal platform for parallel multiplexed sensing with high-density integration.

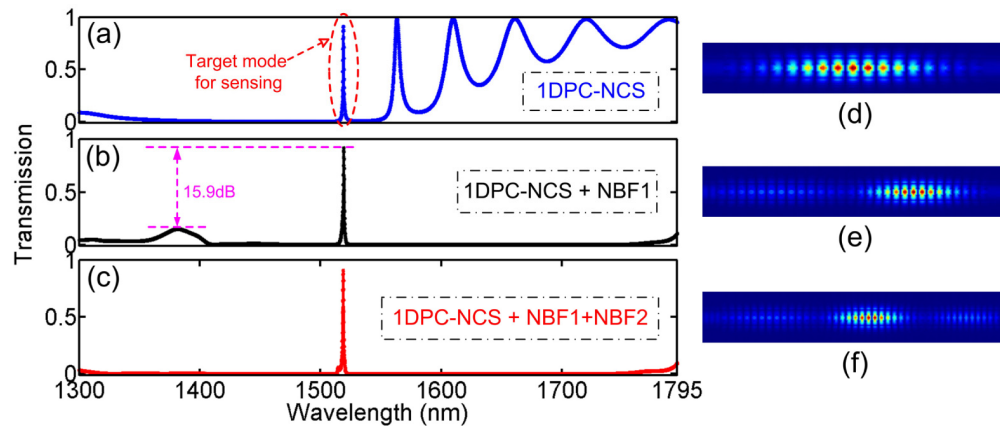


Fig. 3. 3D-FDTD composed transmission spectra and major field distribution profiles ($|E_y|$) in x - y plane of the device formed by (a) and (d) 1DPC-NCS without filter, (b) and (e) series-connected 1DPC-NCS and one 1DPC-NBF1, and (c) and (f) series-connected 1DPC-NCS and two 1DPC-NBFs, respectively. As seen, the additional series-connected 1DPC-NBFs have no effect on the resonant wavelength position of the targeted mode for sensing purpose.

3. Parallel Integrated 1D PC Nanobeam Cavity Sensor Array (PI-1DPC-NCSA) Design

Herein, based on the simulation results shown in Sec. 2 above, with proper engineering of the stop-band of 1DPC-NBF, the displayed method in this work enable to multiplex multiple different resonance 1DPC-NCSs for parallel integrated sensor array design on a monolithic substrate, which is referred to as Parallel Integrated 1D PC Nanobeam Cavity Sensor Array (PI-1DPC-NCSA). The PI-1DPC-NCSA consists of multiple parallel channels. The adjacent channels are separated with air-gap separations. For each channel, three cascaded 1D PC nanobeam sections are employed. One 1DPC-NCS functions as sensing site. And the other two series-connected 1DPC-NBFs function as bandstop filters with different stop-bands. The filters stop-bands are carefully design to avoid any overlap with each other. At the same time, with proper design of the specific targeted resonance of 1DPC-NCS, multi-channel ultra-compact 1D PC nanobeam sensors with different targeted resonances can be multiplexed into a microarray system. Furthermore, in order to restrain crosstalk between channels and to enable all sensing units to be interrogated simultaneously via a single input and output optical fiber lens, all channels are then connected in parallel by using a $1 \times n$ taper-type equal power splitter and a $n \times 1$ S -type power combiner in the input and output port, respectively (here, n is the number of channels). Here, in practical implementations, the beam combiner at the light output could induce non-negligible back reflections and add significant noise into the spectrum. This issue can be partially solved by using a camera or detector array at the output, collecting signals from each channel individually.

Then, to verify the feasibility and suitability of the proposed PI-1DPC-NCSA platform for parallel multiplexed sensing, a 3-channel multiplexed 1DPC-NCSs array containing series-connected 1DPC-NBFs is presented, as shown in Fig. 4. As seen, the presented 1×3 taper-type equal power splitter in the input port consists of a silicon bus waveguide with width $w_{in} = 4.5\mu\text{m}$, and three taper-type branches connecting to a 3-channel PI-1DPC-NCSA. To obtain 3-way equal power division, the width of both top and down taper-type branches is tapered from $1.9\mu\text{m}$ to $0.7\mu\text{m}$, and the width of the middle branch is tapered from $0.7\mu\text{m}$ to $0.7\mu\text{m}$. The length of the three taper-type branches of the splitter is $l_{taper} = 15\mu\text{m}$. In the output port, the presented 3×1 S -type power combiner consists of three S -type waveguides and a silicon bus waveguide with width $w_{out} = 2.1\mu\text{m}$. Between the power splitter and combiner, three channels of the 1D PC nanobeam cavity sensor array are connected in parallel. On each channel, one 1DPC-NCS and two additional 1DPC-NBFs are connected in series. The specific structural

parameters of each channel are as follows: (i) for the first top-channel: $a_1 = 380\text{nm}$, $a_2 = 295\text{nm}$, $a = 330\text{nm}$, $r_1 = r_2 = 90\text{nm}$, $r_{\text{center}} = 131\text{nm}$ and $r_{\text{end}} = 70\text{nm}$. (ii) For the second middle-channel: $a_1 = 392\text{nm}$, $a_2 = 304\text{nm}$, $a = 330\text{nm}$, $r_1 = r_2 = 90\text{nm}$, $r_{\text{center}} = 121\text{nm}$ and $r_{\text{end}} = 85\text{nm}$. (iii) For the third bottom-channel: $a_1 = 404\text{nm}$, $a_2 = 312\text{nm}$, $a = 330\text{nm}$, $r_1 = r_2 = 90\text{nm}$, $r_{\text{center}} = 112\text{nm}$ and $r_{\text{end}} = 85\text{nm}$. The inset on the right side of Fig. 4 is the cross-section of electric field profile for the fundamental TE-like mode propagating through the splitter in y - z plane (transversal surface at the green dashed line).

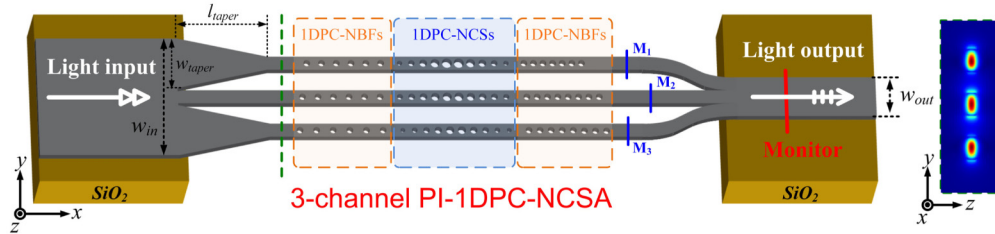


Fig. 4. Schematic of the proposed 3-channel parallel integrated 1D PC nanobeam cavity sensor array (PI-1DPC-NCSA) with single input port and output port. For each channel, three 1D PC nanobeam sections are set in cascade, including one 1DPC-NCS functioned as sensing site and two 1DPC-NBFs functioned as bandstop filters. 1×3 taper-type equal power splitter and 3×1 S-type power combiner are used to split and combine the waveguides in the input port and output port, respectively. The inset on the right side is the cross-section of electric field profile for the fundamental TE-like mode propagating through the splitter in y - z plane (transversal surface at the green dashed line).

By using 3D-FDTD method, the calculated transmission spectrum for each channel of the proposed 3-channel PI-1DPC-NCSA is shown in Figs. 5(a)-5(c), detected by the monitors M_1 , M_2 and M_3 , respectively. As seen, for each channel, a single targeted resonance mode is exhibited in transmission spectrum, indicating that multiple channels can be connected in parallel without resonance overlap. Thus, the multiplexing is quite straightforward by setting n -channel of sensors connected in parallel; therefore, n resonance peaks can be expected. Figure 5(d) shows the combined output transmission spectrum from all three channels. As expected, when 3-channel of sensors are set in parallel ($n = 3$), the transmission spectrum of the sensor array exhibits 3 separated resonant peaks at the wavelengths of $\lambda_1 \sim 1490\text{nm}$, $\lambda_2 \sim 1520\text{nm}$ and $\lambda_3 \sim 1550\text{nm}$. Figures 5(e)-5(g) display the major field distribution profile ($|E_y|$) in x - y plane of the observed targeted mode with the resonance wavelength at λ_1 , λ_2 and λ_3 , respectively. As shown, for each channel, the electric field is strongly localized within the center of the 1DPC-NCS, and is independent of each other and without disturbing.

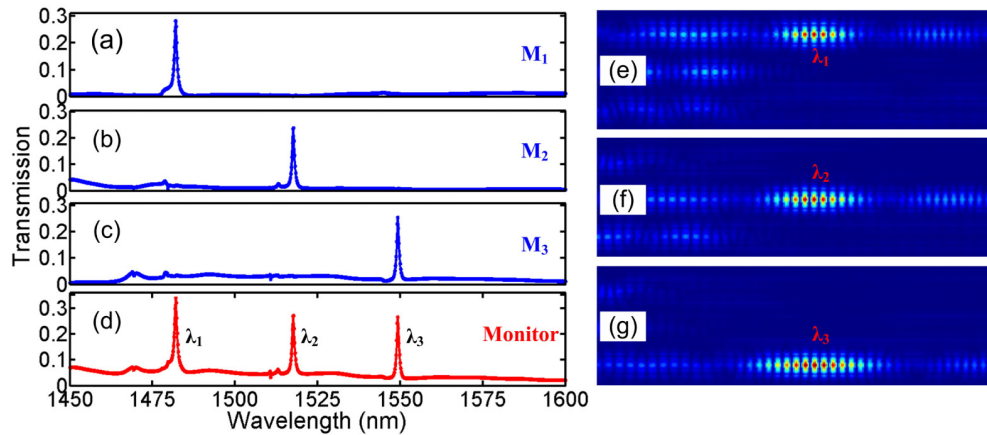


Fig. 5. (a)-(c) 3D-FDTD calculated transmission spectra obtained from each channel containing the specific resonance wavelength at $\lambda_1 \sim 1490\text{nm}$, $\lambda_2 \sim 1520\text{nm}$ and $\lambda_3 \sim 1550\text{nm}$,

respectively. (d) Output transmission spectrum of the proposed 3-channel PI-1DPC-NCSA. (e)-(g) The major field distribution profile ($|E_y|$) in x - y plane of the observed targeted mode with the resonance wavelength at λ_1 , λ_2 and λ_3 , respectively.

Next, to further confirm the independence among each channel and verify the multiplexed sensing performance of the presented 3-channel PI-1DPC-NCSA platform, each channel is independently subjected to five different RI changes (RI-1, RI-2, RI-3, RI-4 and RI-5). With 3D-FDTD calculations, Figs. 6(a) and 6(b) show the composed transmission spectra of the proposed 3-channel PI-1DPC-NCSA when only one sensing channel (*e.g.* top-channel (S_1) and middle-channel (S_2)) is under RI changes, respectively, and the other sensing channels are not. As seen, the corresponding resonance shift in only one sensing mode is evident, and the others remain completely unchanged. This indicates that the multi-resonance modes for sensing are independent of each other; a shift in one of them does not perturb the others, and thus allowing the implementation of simple but functional integrated sensor array for parallel-multiplexing.

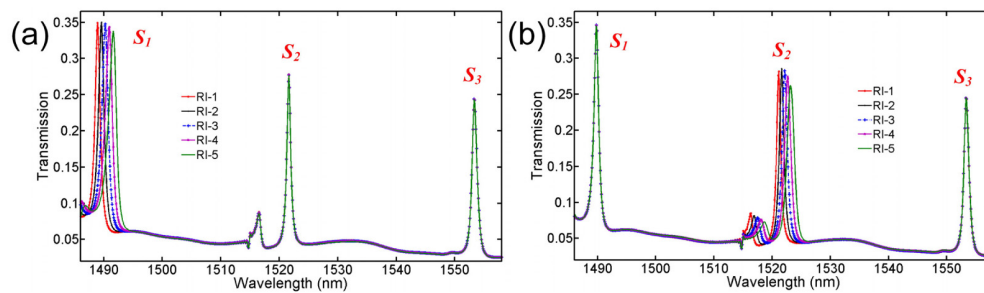


Fig. 6. 3D-FDTD composed transmission spectra observed when three sensing channels are set in parallel and one of them (a) the first top-channel of sensor-1 (S_1), and (b) the second middle-channel of sensor-2 (S_2) is subjected to changes of refractive index (RI) and the others are not.

In fact, the parallel multiplexed use is critical when each nanobeam can be functionalized to respond to a certain perturbation or binding event. Figure 7 shows the composed transmission spectra of the proposed 3-channel PI-1DPC-NCSA when three sensing channels are set in parallel and two of them (i) the first top-channel of sensor-1 (S_1), and (ii) the second middle-channel of sensor-2 (S_2) are independently subjected to different refractive index changes, respectively, and sensor-3 (S_3) is not. As seen, the targeted resonance modes of interest in each of the parallel channels are affected by the changes in the refractive index independently. The numerical results show that the refractive index change reflected by the shifts of resonance frequency S_1 , S_2 , and S_3 are different from each other. Based on this property, multiple different targets can be detected independently at the same time in this parallel scheme.

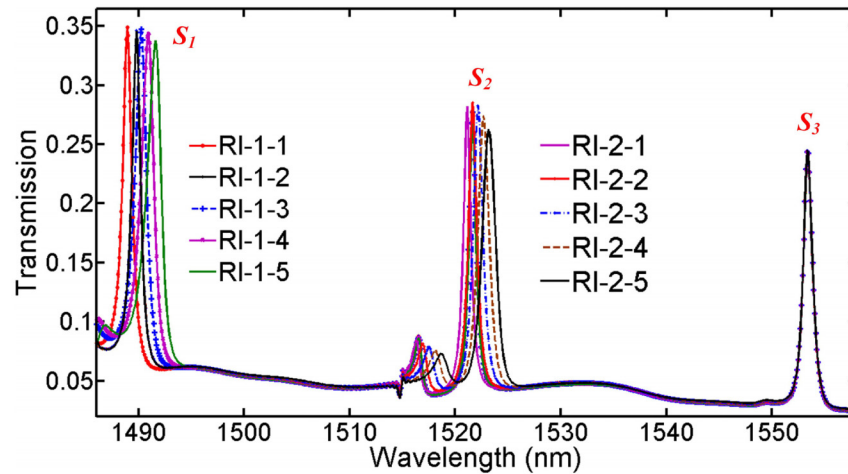


Fig. 7. 3D-FDTD composed transmission spectra observed when three sensing channels are set in parallel and two of them the first top-channel of sensor-1 (S_1), and the second middle-channel of sensor-2 (S_2) are independently subjected to refractive index (RI) changes and the sensor-3 (S_3) is not.

To investigate the RI sensitivities of the proposed sensor array, the device is characterized using a bulk refractive index sensing test. Figure 8(a) shows the composed transmission spectra monitored from the output port of the proposed 3-channel PI-1DPC-NCSA when all the three parallel sensing channels are interrogated simultaneously between a single input and output. As seen above, when the RI value is increased, the resonance of each sensor shifts towards longer wavelengths (red-shift). Figure 8(b) shows the resonant wavelength shifts of each sensor as a function of RI. Linear behaviors can be seen, and the three correlation factors (R^2) are found to be >0.9996 . Based on the simulation results displayed in Fig. 8, the bulk RI sensitivities of each sensor unit can be calculated from the definition of $S = \Delta\lambda/\Delta\text{RI}$, where S is the bulk RI sensitivity, $\Delta\lambda$ is the resonant wavelength (λ_{res}) shift and ΔRI is the surrounding RI change. Thus, the bulk RI sensitivities observed in each sensing-channel from top to bottom (Fig. 4) are $S_1 = 148.5\text{nm}/\text{RIU}$, $S_2 = 121.7\text{nm}/\text{RIU}$, and $S_3 = 112.6\text{nm}/\text{RIU}$, respectively, 1 being the resonant wavelength at shorter wavelength and 3 the resonant wavelength at longer wavelength. Compared to the RI sensitivity ($\sim 60\text{nm}/\text{RIU}$) obtained from [70], the RI sensitivities observed in this work are improved by factor of two. Moreover, it is worth mentioning that without sacrificing Q-factors and RI sensitivities, the footprint of the presented 3-channel PI-1DPC-NCSA is ultra-compact of $4.5\mu\text{m} \times 50\mu\text{m}$ (width \times length), smaller by three orders of magnitude compared to previous sensor arrays based on 2D PC side-coupled cavities [50–52,70]. Thus, the method proposed in this work is attractive and promising in future optical high-density multiplexed sensing and nanophotonic integration. In addition, compared with 2D PC cavity integrated sensor devices, the structures of the proposed single 1D PC nanobeam cavity sensor devices are simpler, and easier to fabricate, which makes it easy to build a lab-on-chip densely integrated sensor array for label-free sensing with high parallel-multiplexing capabilities.

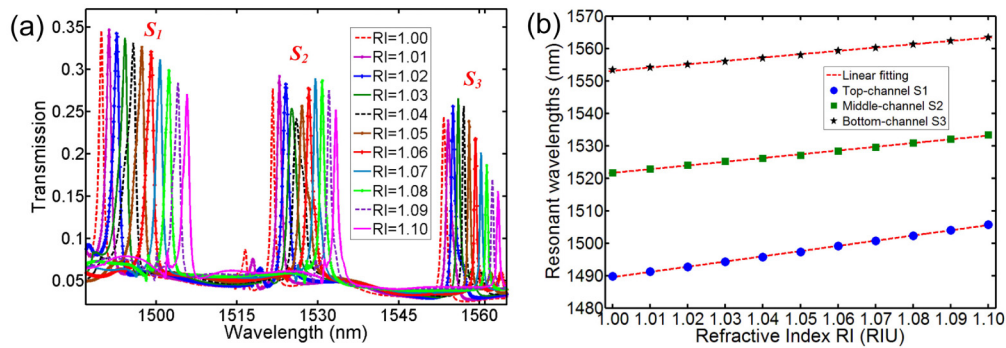


Fig. 8. (a) 3D-FDTD composed transmission spectra monitored from the output port of the proposed 3-channel PI-1DPC-NCSA when all the three parallel sensing channels are interrogated simultaneously between a single input and output. The RI changes from RI = 1.00 to RI = 1.03. (b) Resonant wavelength shifts (red-shifts) of each sensor as a function of RI changes. S_1 , S_2 , and S_3 refer to sensors 1, 2, and 3, respectively, being 1 the resonant wavelength at shorter wavelength and 3 the resonant wavelength at longer wavelength.

Regarding to the feasibility of practical implementations of the proposed scheme in this work, one challenge for high-density sensing application is to interface different nanobeam sensors with different gas channels. In the current design, each sensing unit has a $50\mu\text{m}$ -long footprint, which is achievable with a microfluidic lab-on-a-chip design. Thus, each nanobeam sensing unit can be independently functionalized to respond to a certain perturbation or binding event by using parallel microfluidic channels which can be fabricated with Polydimethylsiloxane (PDMS) by replica molding of a SU8 template [48,66,69]. Finally, the required fabrication accuracy demands electron beam lithography, which is not a scalable fabrication technique for the moment. However, electron beam lithography has shown great improvement in writing speed, and alternative fabrication techniques (deep UV lithography, interference lithography) are promising to generate sub-30 nm fabrication resolution [66]. So, the proposed miniaturized geometries in this work enable multiple 1D PC nanobeam cavity sensors on a monolithic silicon chip. And all sensors can be simultaneously interrogated between a single input fiber lens and a single output fiber lens, from a single optical source.

4. Conclusion

In summary, a method for on-chip parallel multiplexing of integrated 1D photonic crystal nanobeam cavity sensor array has been introduced on a monolithic silicon-on-insulator platform. With 3D-FDTD method, we show that bulk RI sensitivities of $S_1 = 148.5\text{nm}/\text{RIU}$, $S_2 = 121.7\text{nm}/\text{RIU}$, and $S_3 = 112.6\text{nm}/\text{RIU}$ in the 3-channel PI-1DPC-NCSA geometry are obtained. Particularly, the sensor array device footprint is ultra-compact of $4.5\mu\text{m} \times 50\mu\text{m}$, more than three orders of magnitude smaller compared to 2D PC-ISAs. In addition, the numerical results show that PI-1DPC-NCSAs can be strongly coupled to the feeding waveguide with a bus waveguide to coupler. Thus, the displayed PI-1DPC-NCSAs can be easily multiplexed on a chip and interfaced with on-chip integrated optical circuits (with waveguide couplers), making it an ideal system for label-free sensing and achieving high-throughput screening applications. Finally, we believe that the results presented here overcome some of the limitations of 1D PC nanobeam cavity based sensors previously reported (particularly the multiplexing capability), and also improve the dense integration performances of integrated nanophotonic devices and integrated optical circuits (IOC) based on 1D PC nanobeam elements.

Funding

Natural National Science Foundation of China (NSFC) (61501053, 61471050, 61372118); State Key Laboratory of Information Photonics and Optical Communications (IPOC2015ZC03); Fundamental Research Funds for the Central Universities (BUPT); Funds

of Beijing Advanced Innovation Center for Future Internet Technology of Beijing University of Technology, P. R. China.

Acknowledgments

D. Yang wrote the main manuscript text, and prepared all figures. All the authors reviewed the manuscript and discussed the results, drew conclusions and edited the manuscript. D. Yang thanks Dr. Qimin Quan from Rowland Institute at Harvard University and Prof. Yunfeng Xiao from Peking University for useful discussion and helpful comments. Thanks Dr. Anna Shneidman from the group of Prof. Marko Lončar at Harvard University for improving the English of the paper.